

# High Temperature Elastic Properties of Single Crystal Mullite ( $\sim 2.5\text{Al}_2\text{O}_3 \cdot \text{SiO}_2$ ) by Brillouin Spectroscopy

James W. Palko<sup>a</sup>, Ali Sayir<sup>b</sup>, Stanislav V. Sinogeikin<sup>c</sup>, Waltraud M. Kriven<sup>a,\*\*</sup>, Jay D. Bass<sup>c</sup>

a – Department of Materials Science and Engineering, University of Illinois, Urbana, Illinois

b – NASA Glenn Research Center, Cleveland, Ohio

c – Department of Geology, University of Illinois, Urbana, Illinois

## Abstract

The complete elastic tensor of mullite has been determined by brillouin spectroscopy at room temperature and elevated temperatures up to 1200 °C. Equivalent, isotropic moduli (bulk, shear, and Young's) have been calculated. The room temperature values obtained using Voigt-Reuss-Hill averaging are:  $K_{\text{VRH}} = 173.5 \pm 6.9$  GPa,  $G_{\text{VRH}} = 88.0 \pm 3.5$  GPa,  $E_{\text{VRH}} = 225.9 \pm 9.0$  GPa. All moduli show relatively gradual decreases with temperature. The temperature derivatives obtained for the equivalent, isotropoic moduli are:  $dK_{\text{VRH}}/dT = -17.5 \pm 2.5$  MPa/°C,  $dG_{\text{VRH}}/dT = -8.8 \pm 1.4$  MPa/°C,  $dE_{\text{VRH}}/dT = -22.6 \pm 2.8$  MPa/°C. Substantial differences between bulk properties calculated from the single crystal measurements in this study and the properties reported in the literature for polycrystalline sintered mullite are identified, indicating the importance of factors such as microstructure, intergranular phases, and composition to the elasticity of mullite ceramics.

---

\*\* - Fellow American Ceramic Society

## I. Introduction

Mullite is found in many common ceramics. More recently it has gained favor for use in advanced materials such as structural ceramic matrix composites as both a matrix and reinforcing phase. It has such desirable qualities as high temperature stability and oxidation resistance that give it potential for use in many applications<sup>1</sup> such as gas turbine engines.<sup>2</sup>

Because of the long-term use of mullite and its technological importance,<sup>3</sup> many measurements have been made of its mechanical properties, including measurements of its elastic properties at ambient and elevated temperatures.<sup>4-10</sup> These have all concentrated, however, on bulk polycrystalline properties, and there are great discrepancies in the measured values.

Recently, mullite has become available in single-crystal or highly textured polycrystalline fiber form by use of a laser-heated float zone crystal growth technique.<sup>11</sup> Such samples allow measurement of the single-crystal elastic properties of mullite. These measurements provide useful property data for the design of components using single crystals (e.g. single crystal reinforcing fibers). They also yield information as to what degree the elastic properties of mullite ceramics are a result of the intrinsic properties of the mullite crystal as compared to characteristics that may depend on processing such as microstructure, and intergranular phases which are common in sintered mullite. Therefore, a detailed understanding of the single crystal elastic properties of mullite is extremely useful for a fundamental understanding of the mechanical properties of complex, alumino-silicate ceramics. Such single crystal measurements are made in this study using Brillouin scattering.

Recently, we have reported a full single crystal elastic tensor for mullite at room temperature and selected constants ( $C_{11}$ ,  $C_{33}$ ,  $C_{44}$ ,  $C_{55}$ ) to 1400°C using Brillouin spectroscopy.<sup>12</sup>

Orientation of the samples in the previous work was based on sample morphology and symmetry of the velocity data itself, and the previous study utilized a large rigidly mounted furnace that allowed access to only a few phonon directions with limited knowledge of the sample orientation at high temperature. This work gives a more accurate room temperature tensor than the previous work, due to a refinement of the sample crystal orientations by X-ray diffraction, as well as the temperature dependence of the full tensor to 1200 °C also with improved accuracy made possible by the use of a compact furnace design that allows collection of multiple phonon directions without remounting the sample.<sup>13</sup> Neutron diffraction to 1650 °C and X-ray diffraction to 900 °C of polycrystalline or unconstrained powdered mullite with a composition of  $3\text{Al}_2\text{O}_3 \cdot 2\text{SiO}_2$  was also reported in the previous work. This data was used to calculate thermal expansion for the previous study. For the current study, thermal expansion was taken from an X-ray study of mullite with composition  $2\text{Al}_2\text{O}_3 \cdot \text{SiO}_2$  to 900 °C because of its closer composition to the current sample.<sup>14</sup>

## II. Theory

Brillouin scattering is the inelastic scattering of light from acoustic waves, allowing the determination of the wave speed. It provides an ideal probe of the elastic properties of the single crystal mullite samples available (especially at high temperatures), requiring only small sample volumes (e.g. 100 x 100 x 50  $\mu\text{m}$ ) and no physical contact with the sample. It is capable of measuring the phonon velocities along many propagation directions in a single sample. Brillouin scattered light is shifted in frequency with respect to the incident light by a factor that is proportional to the velocity of the acoustic waves (Eq. 1).<sup>15</sup>

$$V = \left( \frac{\Delta\omega}{\omega} \right) \left( \frac{c}{2n \sin\left(\frac{\theta}{2}\right)} \right) \quad (1)$$

Here  $V$  is the velocity of the acoustic wave,  $\Delta\omega$  is the frequency shift of the scattered light,  $\omega$  is the frequency of the incident light,  $c$  is the speed of light,  $n$  is the index of refraction of the sample, and  $\theta$  is the scattering angle.

For this study, platelet geometry is used such that the sample has flat, parallel faces, the phonon propagates in the plane of the sample, and the face normals, incident, and scattered light rays all lie within a plane.<sup>16</sup> Figure 1 gives a schematic of the platelet scattering geometry. With the symmetric platelet geometry, the scattering angle is easily defined, and no knowledge of the index of refraction of the sample is necessary. This is particularly beneficial for high temperature studies where the variation of index of refraction with temperature is generally unknown and difficult to measure.

The elastic waves probed may be treated by a continuum mechanics analysis that relates wave velocities along a given crystallographic direction to the elastic moduli and density of the material via Christoffel's equation (Eq. 2).<sup>17</sup>

$$\left| C_{ijkl} q_j q_l - \rho V^2 \delta_{ik} \right| = 0 \quad (2)$$

$C$  is the elasticity tensor for the material,  $q$  is a unit vector along the path of phonon propagation,  $\rho$  is the density, and  $\delta$  is the Kröneckers delta function. Since mullite is orthorhombic, 9 independent elastic constants ( $C_{11}$ ,  $C_{22}$ ,  $C_{33}$ ,  $C_{44}$ ,  $C_{55}$ ,  $C_{66}$ ,  $C_{12}$ ,  $C_{13}$ ,  $C_{23}$ ) are required to describe its elastic tensor (represented here in Voigt notation).

### III. Experimental Procedure

#### *(1) Brillouin Scattering System*

For this study, an  $\text{Ar}^+$  laser with a wavelength of 514.5 nm is used to illuminate the sample. Scattered light is analyzed by a 6-pass tandem Fabry-Perot interferometer. Figure 2 is a schematic of the system used to collect Brillouin spectra. The operation of the interferometer has been detailed elsewhere.<sup>18,19</sup>

Room temperature work is performed with a  $90^\circ$  scattering angle. An Eulerian cradle is used to rotate the sample around its face normal to access different phonon directions. The high temperature results of this study are obtained using a compact furnace mounted on the Eulerian cradle, allowing multiple phonon directions to be collected without remounting the sample. The construction and operation of this furnace is described elsewhere.<sup>13</sup> An  $80^\circ$  scattering angle is used for the high temperature work.

#### *(2) Sample Preparation*

Samples are taken from a fiber grown using the laser-heated, float zone method<sup>11</sup>. For preparation of the source rod, high purity (99.99% pure) polycrystalline alumina powder was

obtained from CERAC/pure\* (325 mesh) and 99.99 % pure  $\text{SiO}_2$  from Alpha Products. The starting composition was chosen close to the 3:2 molar ratio of  $\text{Al}_2\text{O}_3$  :  $\text{SiO}_2$  and was 70.4 wt %  $\text{Al}_2\text{O}_3$ . The fibers characterized were from a second pass through the laser. Figure 3 shows side and cross sectional views of a representative mullite fiber. A definite growth face is apparent, forming a sawtooth pattern. X-ray analysis shows this to be the (010) face. Cleavage is occasionally observed along this plane, as is observed in natural mullite and sillimanite samples.<sup>20</sup> The fiber has a roughly elliptical cross section minus the growth facet. The roughness on the surface in Figure 3 (b) is due to the diamond saw cutting process. The fiber is for the most part optically clear, with occasional white streaks across its width, apparently consisting of bubbles or occlusions. These white streaks often coincide with the points of the sawtooth pattern along the fiber edge.

Separate platelets for velocity measurements with approximate face normals of  $\sim[0\ 1\ 0]$ ,  $\sim[0\ 0\ 1]$ , and  $\sim[0.9744\ 0.2250\ 0]$  were ground using a series of diamond and SiC abrasives ranging from 30 to 1  $\mu\text{m}$ . (Normals and planes are given in an equidistant Cartesian coordinate system, not the orthorhombic lattice of mullite.) Machine grinding was used for some of the coarser steps and the finer polishing was completed by hand. Glass was placed around the sample as a sacrificial material to minimize rounding of the sample faces, which was less than  $1.5^\circ$  for the entire included angle of the face (usually  $< 1^\circ$ ). Nonparallelness between the faces was less than  $0.5^\circ$ , and the faces produced had a mirror finish with very few scratches visible at 40x magnification. Final dimensions of the samples taken lengthwise from the fiber,  $\sim(100)$  and  $\sim(010)$ , were approximately 3 mm x 0.4 mm x 0.25 – 0.1 mm. Cross sectional samples,  $\sim(001)$ ,

---

\* - Ceralox Corp., Tucson, AZ 08576

had approximate diameters of 0.4 mm and thicknesses of 0.15 –0.1 mm. The orientations of the sample platelets were determined using X-ray precession photography.<sup>21</sup>

## IV. Results

### *(1) Sample Characterization*

The fiber shows uniform extinction under cross polarized light when the polarization direction is nearly aligned or perpendicular to the fiber axis, regardless of rotation about this axis. When ground with parallel faces, some variation in interference color is noted occurring in bands across some samples. This may be a result of a slight change in index of refraction due to compositional variations (or possibly slight variations in thickness). Extinction is somewhat less uniform in cross sections of the fiber.

The composition of the mullite was determined with an electron microprobe (wavelength dispersive) using natural kyanite as a standard. The average composition is listed in Table I along with unit cell parameters determined by X-ray diffraction for the mullite sample. The error quoted for composition is the standard deviation of values measured at 10  $\mu\text{m}$  intervals along the length of a fiber section and 5  $\mu\text{m}$  intervals across its width. Density is determined using Eq. 3 for the chemical formula of the unit cell.<sup>22</sup>



x is the average number of oxygen vacancies per unit cell. It is related to the  $\text{Al}_2\text{O}_3/\text{SiO}_2$  molar ratio,  $n(\text{Al}_2\text{O}_3/\text{SiO}_2)$  by Eq. 4.

$$x = \frac{2n(\text{Al}_2\text{O}_3/\text{SiO}_2) - 2}{2n(\text{Al}_2\text{O}_3/\text{SiO}_2) + 1} \quad (4)$$

Initial X-ray diffraction analysis was performed using a four-circle diffractometer and shows that the sample is actually a very highly textured polycrystal, as seen in Figure 4. This analysis verifies that the crystallites have orthorhombic symmetry with slightly varying orientations defined by small rotations about the c axis, which is coincident with the fiber axis. All the crystallites found lie within  $5^\circ$  of each other and the majority lie within  $2^\circ$ . There is no resolvable splitting in the c axis peaks. Lattice parameters for the sample are calculated by fitting the major peak for each scan. A total of six peaks are used in the calculation: (040), (400), (002), (402), (042), (222). The errors quoted encompass all cell parameters calculated with five of the six peaks (i.e. the maximum and minimum values from six calculations with five peaks). The calculated unit cell angles deviate slightly from  $90^\circ$  ( $\alpha = 90.4174^\circ$ ,  $\beta = 90.2971^\circ$ ,  $\gamma = 89.8230^\circ$ ), probably due to the small peaks in close proximity resulting from the highly oriented polycrystalline nature of the sample and large sample size. For the purpose of calculating the cell volume, the interaxial angles were fixed to  $\alpha = \beta = \gamma = 90^\circ$ . The sample characterized in Table I is the same as that in the previous study, but the inclusion of some additional X-ray data resulted in a slight (0.6%) decrease in calculated volume.

## *(2) Room Temperature Elasticity*



The full set of 9 room temperature, elastic moduli (Table II) have been determined using a linearized least-squares inversion procedure based on 158 separate velocities measured along 37 different crystallographic directions in three different planes (Figures 5, 6, and 7). This algorithm calculates velocities based on an initial set of preliminary  $C_{ij}$ 's (Eq. 2) along the same phonon propagation directions as those measured and then varies the elastic moduli so as to minimize the misfit between the calculated and measured velocities.<sup>23</sup> Velocities calculated from the moduli obtained appear as solid curves in Figures 5, 6, and 7. We note that the final best-fit solution is highly insensitive to the starting guess for the  $C_{ij}$ 's. Equivalent, isotropic moduli have been calculated using the Voigt, Reuss, and Voigt-Reuss-Hill averaging schemes (denoted by V, R, and VRH subscripts) and are listed in Table II.

The errors in Table II refer purely to the statistical error in the fit. Deviations from the nominal sample normals ( $\sim[0\ 1\ 0]$ ,  $\sim[0\ 0\ 1]$ ,  $\sim[0.9744\ 0.2250\ 0]$ ) are less than  $\sim 4^\circ$  for all samples. The higher symmetry sample normals are retained to simplify calculation of moduli and error analysis. Rotation about the sample normal is determined by extinction under cross polarized light and is considered accurate to  $\pm 3^\circ$ . The error resulting from misorientation of the sample (including rotation about the sample plane normal) is estimated to be less than  $\pm 2\%$  of the calculated moduli. This estimate is based on including deviations in each axis of the sample plane normal and each rotation singly and assuming additivity. (Rotations are calculated with sample plane normals of  $[1\ 0\ 0]$ ,  $[0\ 1\ 0]$ , and  $[0\ 0\ 1]$  for simplicity.) The uncertainty in density, on which the moduli are directly proportional, is  $\pm 0.7\%$ .

### *(3) High Temperature Elasticity*

For high temperature moduli determinations, velocities were collected from each sample plane at 200 °C increments to 1200 °C. Figures 8, 9, and 10 show the calculated elastic longitudinal (e.g.  $C_{11}$ ), shear (e.g.  $C_{44}$ ), and cross (e.g.  $C_{12}$ ) moduli along with best fit, least squares regression lines. High temperature constants are calculated at each temperature from 16 velocities collected along 9 directions (3 in each sample plane; one along each projection of the principle axes and one 45° between them). Linear temperature dependencies are suggested for all single crystal moduli, with the possible exception of  $C_{23}$  which shows a large scatter with temperature. Linear decreases in  $E_{VRH}$ ,  $G_{VRH}$ , and  $K_{VRH}$  are also indicated (Figures 11, 12, 13).

The high temperature constants are calculated directly from Eq. 2 using the same sample face normals as the room temperature calculations.  $C_{12}$  and  $C_{13}$  are determined from a weighted average of a single shear and longitudinal acoustic modes based on the sensitivity of the moduli to the specific velocity.<sup>21</sup>  $C_{23}$  is calculated only from the longitudinal mode due to difficulty in assigning a specific shear mode. This may account for some of the scatter in the data. A volume coefficient of thermal expansion of  $15.8 \times 10^{-6} / ^\circ\text{C}$  for  $2\text{Al}_2\text{O}_3 \cdot \text{SiO}_2$  mullite is used for the calculation of density at high temperature as obtained from the sum of linear expansion coefficients of the lattice parameters given by Schneider and Eberhard.<sup>14</sup> This value was determined from measurements only to 900 °C. Because of the lower temperature limit for this study (1200 °C) as compared to the previous one (1400 °C), it was decided that the extrapolation in temperature is more acceptable than the greater difference in composition. The temperature derivatives of the single crystal moduli and Voigt-Reuss-Hill average moduli are given in Table III. Errors quoted refer to the 95% confidence intervals for the slope of the linear fit.

## V. Discussion

### *(1) Room Temperature Elasticity*

The single-crystal moduli, for the most part, fall within the error bars of those previously reported.<sup>12</sup> The one significant discrepancy is  $C_{23}$  which was previously reported as 135 GPa based on an orientation resulting from the symmetry of the velocity data itself. The current reorientation represents a rotation of  $13^\circ$  (around the  $c$  axis) for one plane,  $\sim(100)$ , which strongly affects  $C_{23}$ . The current value (142.3 GPa) is  $\sim 5\%$  higher and is considered the more accurate due to the precision of the X-ray orientation. The other constants are clearly affected much less by this reorientation. This occurs since the other constants depend very weakly on this rotation (Eq. 2). Cross constants such as  $C_{23}$  are generally the most strongly affected by misorientation.<sup>24</sup>

Sillimanite,  $\text{Al}_2\text{SiO}_5$ , which has a very similar crystal structure to mullite<sup>25</sup>, shows similar elastic behavior. The relative magnitudes of the moduli by value is the same for both crystals, except for the exchange of  $C_{13}$  and  $C_{66}$ . Andalusite shows the same order in longitudinal constants when its  $a$  and  $b$  axes are exchanged, which is the transformation required to bring its structure into closest correspondence with mullite<sup>25</sup>. The bulk properties calculated for mullite and sillimanite (Table II) are similar, while andalusite has a smaller bulk modulus but larger shear and Young's moduli.

Bulk values calculated here for mullite agree well with the recent measurements of a polycrystalline mullite sample by Ledbetter et al.<sup>10</sup>, as well as the polycrystalline Young's modulus measurements of Pentry<sup>7</sup>. There are, however, considerable differences among some of the values of elastic moduli reported for polycrystalline mullite (Table IV), and certain authors<sup>8,9</sup>

have reported values that exceed even the Voigt bounds of the respective moduli calculated here. These should set an upper limit on the possible values for a polycrystalline aggregate of mullite. The discrepancy may be due to intergranular phases. Compositional differences may also play a role. The polycrystalline studies were performed on mullite samples with a lower alumina content ( $3 \text{ Al}_2\text{O}_3 \cdot 2 \text{ SiO}_2$ ).

## *(2) High Temperature Elasticity*

Comparisons with temperature derivatives of polycrystalline elastic properties given in the literature show significant differences (Table V). The derivative obtained for Young's modulus in this study is more negative than  $-8 \text{ MPa}/^\circ\text{C}$  as seen in the data of Wachtman for temperatures below  $600^\circ\text{C}$ <sup>5</sup>. (Note that the scale in Figure 11 for the literature data is twice as fine than for the current data, while in Figure 12 it is twice as coarse.) Ledbetter also reports a more gradual decrease in Young's modulus ( $-11 \text{ MPa}/^\circ\text{C}$ )<sup>10</sup>. These differences could result from a glassy phase in the polycrystalline body. Silica glass is known to stiffen with temperature<sup>26</sup>. A similar effect may occur with an intergranular glass phase, thereby mitigating the reduction in stiffness of the mullite grains. The temperature derivative of the shear modulus from the present study, however, is much smaller than  $-30 \text{ MPa}/^\circ\text{C}$  which is suggested by a linear fit to Wygant's data.<sup>4</sup> This may be due to a low melting (or more rapidly softening) intergranular phase. Ledbetter reports an extremely gradual  $-3.3 \text{ MPa}/^\circ\text{C}$  temperature derivative of shear modulus as well as a bulk modulus temperature derivative of  $-20 \text{ MPa}/^\circ\text{C}$ <sup>10</sup>. All values from Ledbetter are for room temperature and are corrected to zero porosity. The temperature behavior of mullite ceramics is clearly affected, and possibly dominated, by properties other than those intrinsic to the crystalline mullite itself.

## VI. Conclusions

The full elastic tensor of mullite has been determined at room and elevated temperatures to 1200 °C. Room temperature values show close correspondence with structural analogs, sillimanite and andalusite. Bulk elastic properties calculated from the single crystal moduli agree well with some measurements on polycrystalline mullite<sup>7,10</sup>, but there are substantial differences with much published data. In particular some authors report values<sup>8,9</sup> that exceed the maximum possible limit (Voigt bound) for average moduli calculated here, suggesting that intergranular phases and composition may play a very large role in determining the elastic properties of nominally pure mullite ceramics.

High temperature measurements were made in 200 °C intervals to 1200°C. A relatively gradual linear decrease was noted in all moduli with temperature. The temperature derivatives of bulk properties calculated from the single crystal moduli do not correspond well with much of the data in literature, again suggesting that intergranular phases are important in the elasticity of mullite ceramics. Phases having behavior at high temperature much different than mullite, such as stiffening or rapid softening with temperature, are suggested by this data.

## Acknowledgments:

The work of J. W. Palko was supported by the Fannie and John Hertz Foundation graduate fellowship. X-ray work was performed by J. McMillan at the Center for Microanalysis of Materials at UIUC. Electron microprobe analysis was conducted by Dr. I. Steele at the

University of Chicago. This work was partially supported by a United States Air Force Office of Scientific Research AASERT Grant, under contract number F49620-97-1-0427 and NSF grant EAR-96-14416. The development of new fibers was supported by the United States Air Force Office of Scientific Research under contract number F49620-00-1-0048 and NASA cooperative agreement NCC3-372.

## References

- 1 I. A. Aksay, D. M. Dabbs, and M. Sarikaya, "Mullite for Structural, Electronic, and Optical Applications," *J. Am. Ceram. Soc.* **74** [10] 2343-2358 (1991).
- 2 U. Steinhäuser, W. Braue, J. Göttring, B. Kanka, and H. Schneider, "A New Concept for Thermal Protection of All-Mullite Composites in Combustion Chambers," *J. Europ. Ceram. Soc.* **20** 651-658 (2000).
- 3 A. J. Skoog and R. E. Moore, "Refractory of the Past for the Future: Mullite and Its Use as a Bonding Phase," *Am. Ceram. Soc. Bull.* **67** [7] 1180-1185 (1988).
- 4 J. F. Wygant, "Elastic and Flow Properties of Dense, Pure Oxide Refractories," *J. Am. Ceram. Soc.* **34** [12] 374-380 (1951).
- 5 J. B. Wachtman and D. G. Lam, "Young's Modulus of Various Refractory Materials as a Function of Temperature," *J. Am. Ceram. Soc.* **42** [5] 254-260 (1959).
- 6 J. E. Fenstermacher and F. A. Hummel, "High-Temperature Mechanical Properties of Ceramic Materials: IV Sintered Mullite Bodies," *J. Am. Ceram. Soc.* **44** [6 June] 284-289 (1961).
- 7 R. A. Pentry, D. P. H. Hasselman, and R. M. Spriggs, "Young's Modulus of High-Density Polycrystalline Mullite," *J. Am. Ceram. Soc.* **55** 169-170 (1972).
- 8 M. G. M. U. Ismail, Z. Nakai, and S. Shigeyuki, "Microstructure and Mechanical Properties of Mullite Prepared by the Sol-Gel Method," *Comm. Am. Ceram. Soc.* **70** [1] C7-8 (1987).

- 9 W. H. Kelly, A. N. Palazotto, R. Ruh, J. K. Heuer, and A. Zangvil, "Thermal Shock Resistance of Mullite and Mullite-ZrO<sub>2</sub>-SiC Whisker Composites," *Ceram. Engr. & Sci. Proc.* **18** [3] 195-203 (1997).
- 10 H. Ledbetter, S. Kim, D. Balzar, S. Crudele, and W. Kriven, "Elastic Properties of Mullite," *J. Am. Ceram. Soc.* **81** [4] 1025-1028 (1998).
- 11 A. Sayir and S. C. Farmer, "Directionally Solidified Mullite Fibers," *Mat. Res. Soc. Sym. Proc.* **365** 11-20 (1995).
- 12 W. M. Kriven, J. W. Palko, S. Sinogeikin, J. D. Bass, A. Sayir, G. Brunauer, H. Boysen, F. Frey, and J. Schneider, "High Temperature Single Crystal Properties of Mullite," *J. Europ. Ceram. Soc.* **19** 2529-2541 (1999).
- 13 S. V. Sinogeikin, J. M. Jackson, B. O'Neill, J. W. Palko, and J. D. Bass, "Compact High-Temperature Cell for Brillouin Scattering Measurements," *Rev. Sci. Instrum.* **71** [1] 201-206 (2000).
- 14 H. Schneider and E. Eberhard, "Thermal Expansion of Mullite," *J. Am. Ceram. Soc.* **73** [7] 2073-2076 (1990).
- 15 G. B. Benedek and K. Fritsch, "Brillouin Scattering in Cubic Crystals," *Phys. Rev.* **149** [2] 647-662 (1966).
- 16 E. S. Zouboulis and M. Grimsditch, "Refractive Index and Elastic Properties of Single-crystal Corundum ( $\alpha$ -Al<sub>2</sub>O<sub>3</sub>) up to 2100 K," *J. Appl. Phys.* **70** [2] 772-776 (1991).
- 17 L. D. Landau and E. M. Lifshitz, *Theory of Elasticity* (Pergamon Press, London, 1959), p. 104.
- 18 J. D. Bass, "Elasticity of Grossular and Spessartite Garnets by Brillouin Spectroscopy," *J. Geophys. Res.* **94** 7621-7628 (1989).
- 19 S. V. Sinogeikin, J. D. Bass, and T. Katsura, "Sound Velocities and Elastic Properties of Fe-bearing Wadsleyite and Ringwoodite," *J. Geophys. Res.* **103** [B9] 20,819-825 (1998).

- 20 W. D. Nesse, *Introduction to Optical Mineralogy* (Oxford University Press, New York, 1986), p. 170-171.
- 21 J. Palko, M.S. Thesis, University of Illinois, Urbana-Champaign, 2000.
- 22 W. M. Kriven and J. A. Pask, "Solid Solution Range and Microstructure of Melt-Grown Mullite," *J. Am. Ceram. Soc.* **66** [9] 649-654 (1983).
- 23 D. J. Weidner and H. R. Carleton, "Elasticity of Coesite," *J. Geophys. Res.* **82** [8] 1334-1346 (1977).
- 24 R. P. Ingel and D. Lewis, "Errors in Elastic Constant Measurements in Single Crystals," *J. Am. Ceram. Soc.* **71** [4] 261-264 (1988).
- 25 H. Schneider, K. Okada, and J. A. Pask, *Mullite and Mullite Ceramics* (John Wiley & Sons, Chichester, 1994), p. 1-8.
- 26 J. D. Bass, "Elasticity of Minerals, Glasses, and Melts"; pp. 45-63 in *Mineral Physics and Crystallography: A Handbook of Physical Constants*. edited by T. J. Ahrens (American Geophysical Union, Washington, DC, 1995).
- 27 M. T. Vaughan and D. J. Weidner, "The Relationship of Elasticity and Crystal Structure in Andalusite and Sillimanite," *Phys. Chem. Miner.* **3** 1-12 (1978).
- 28 M. I. Osendi, B. A. Bender, and D. Lewis, III, "Microstructure and Mechanical Properties of Mullite-Silicon Carbide Composites," *J. Am. Ceram. Soc.* **72** [6] 1049-1054 (1989).



Figure 1: Schematic of platelet scattering geometry

Figure 2: Schematic of Brillouin scattering system.

Figure 3: Optical micrographs of mullite sample (a) lengthwise and (b) in cross section

Figure 4: X-ray scan rotating sample around fiber axis with fixed  $2\theta$

Figure 5: Room temperature velocities versus rotation in  $\sim(100)$  plane

Figure 6: Room temperature velocities versus rotation in  $\sim(010)$  plane

Figure 7: Room temperature velocities versus rotation in  $\sim(001)$  plane

Figure 8: Single-crystal longitudinal moduli versus temperature

Figure 9: Single-crystal shear moduli versus temperature

Figure 10: Single-crystal cross moduli versus temperature

Figure 11: Young's modulus of mullite versus temperature

Figure 12: Shear modulus of mullite versus temperature

Figure 13: Bulk modulus of mullite versus temperature

Table I: Properties of mullite sample at room temperature

<b>a (nm)</b>	$0.758 \pm 0.001$
<b>b (nm)</b>	$0.767 \pm 0.001$
<b>c (nm)</b>	$0.289 \pm 0.001$
<b>Cell Volume (nm<sup>3</sup>)</b>	$0.168 \pm 0.001$
<b>Molar Al<sub>2</sub>O<sub>3</sub>/SiO<sub>2</sub> ratio</b>	$2.5 \pm 0.1$
<b>Theoretical Density (g/cm<sup>3</sup>)</b>	$3.11 \pm 0.02$

Table II: Room temperature moduli of mullite, andalusite, and sillimanite

Constant	Mullite	Sillimanite <sup>27</sup>	Andalusite <sup>27</sup>
$C_{11}$ (GPa)	$281.9 \pm 0.7$	287.3	233.4
$C_{22}$ (GPa)	$244.2 \pm 0.9$	231.9	289.0
$C_{33}$ (GPa)	$363.6 \pm 1.0$	388.4	380.1
$C_{44}$ (GPa)	$111.7 \pm 0.6$	122.4	99.5
$C_{55}$ (GPa)	$78.2 \pm 0.5$	80.7	87.8
$C_{66}$ (GPa)	$79.2 \pm 0.5$	89.3	112.3
$C_{12}$ (GPa)	$105.1 \pm 1.0$	94.7	81.4
$C_{13}$ (GPa)	$100.3 \pm 1.3$	83.4	116.2
$C_{23}$ (GPa)	$142.3 \pm 1.6$	158.6	97.7
$K_V$ (GPa)	176.1	175.1	165.9
$K_R$ (GPa)	171.0	166.4	158.0
$K_{VRH}$ (GPa)	173.5	170.8	162.0
$G_V$ (GPa)	90.0	95.1	100.4
$G_R$ (GPa)	86.1	87.8	97.7
$G_{VRH}$ (GPa)	88.0	91.5	99.1
$E_V$ (GPa)	230.6	241.6	250.6
$E_R$ (GPa)	221.2	224.0	243.0
$E_{VRH}$ (GPa)	225.9	232.8	246.8

Table III: Fitted temperature derivatives for mullite to 1200°C

Modulus	Temperature derivative (MPa/°C)
$C_{11}$	$-29.2 \pm 3.2$
$C_{22}$	$-29.7 \pm 1.6$
$C_{33}$	$-28.6 \pm 4.2$
$C_{44}$	$-7.9 \pm 1.1$
$C_{55}$	$-6.5 \pm 0.9$
$C_{66}$	$-10.1 \pm 0.9$
$C_{12}$	$-16.1 \pm 0.5$
$C_{13}$	$-6.8 \pm 1.4$
$C_{23}$	$-8.1 \pm 10.5$
$K_{VRH}$	$-17.5 \pm 2.5$
$G_{VRH}$	$-8.8 \pm 1.4$
$E_{VRH}$	$-22.6 \pm 2.8$

Table IV: Bulk properties of polycrystalline mullite reported in literature

E (GPa)	$\nu$	G (GPa)	K (GPa)	Density	Ref.
225.9		88.0	173.5	3110 kg/m <sup>3</sup>	Pres. Study (VRH Aver.)
		59			4
143.0				2780 kg/m <sup>3</sup>	5
124					6
223.4 $\pm$ 5.5				Corrected to 100% (Spriggs)	7
224.1 $\pm$ 5.5				Corrected to 100% (Hasselman)	“
246				>98% (3150 kg/m <sup>3</sup> )	8
194	0.276	76.0	144.3	95%	28
252	0.266	99.5	179.5		9
227.5	0.280	88.9	172.4	99.6%	10
229.1	0.280	89.5	173.9	Corrected to 100%	“

Table V: Comparison of temperature derivatives with literature values

$dK/dT$ (MPa/°C)	$dG/dT$ (MPa/°C)	$dE/dT$ (MPa/°C)	Ref.	Notes
$-17.5 \pm 2.5$	$-8.8 \pm 1.4$	$-22.6 \pm 2.8$	Pres. Study	VRH average
				20 – 1200 °C
		-8	5	20 – 600 °C
-20	-3.3	-11	10	
	-30		4	

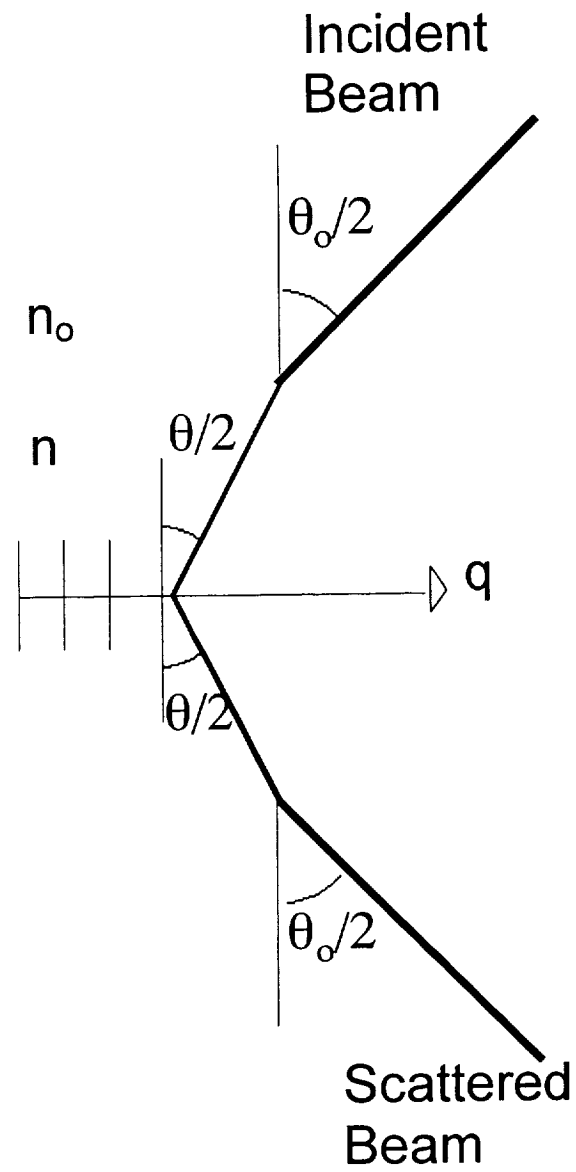


Figure 1: Schematic of platelet scattering geometry

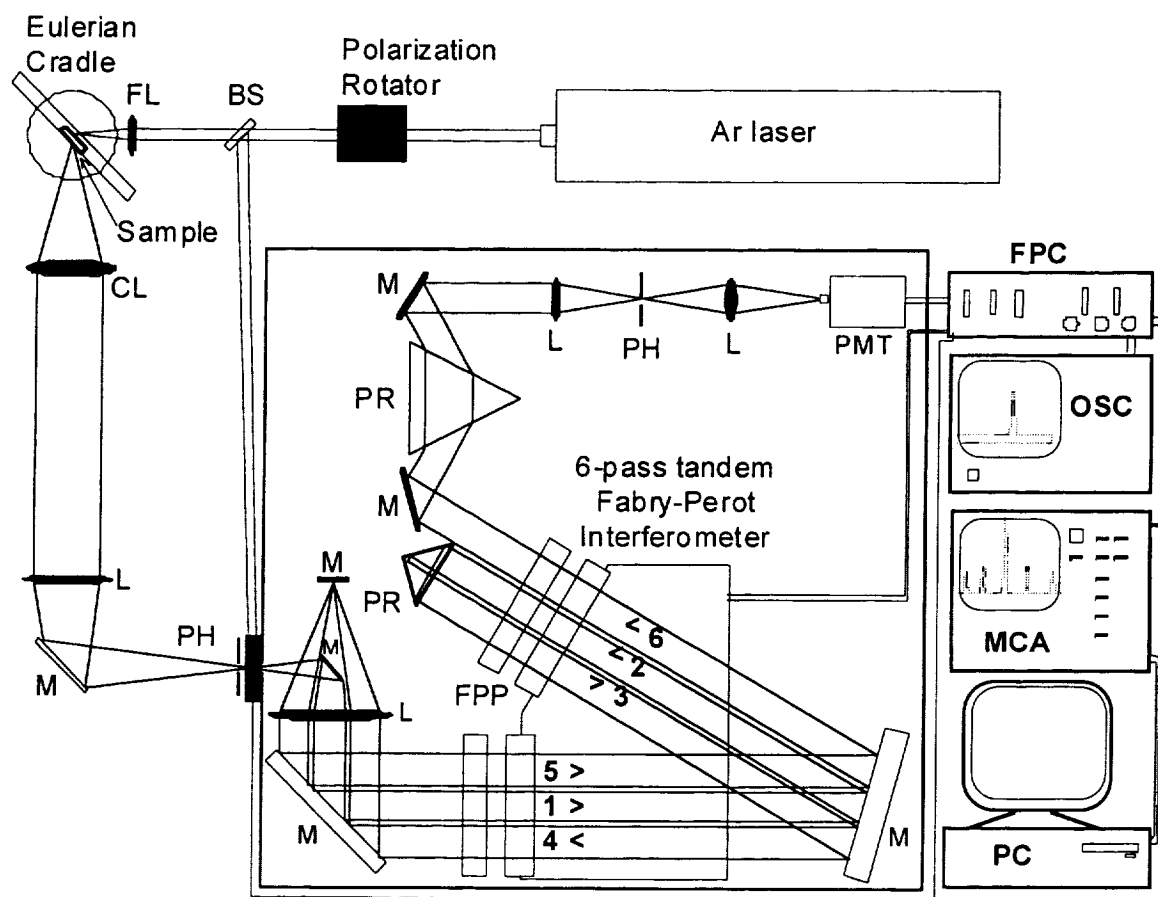
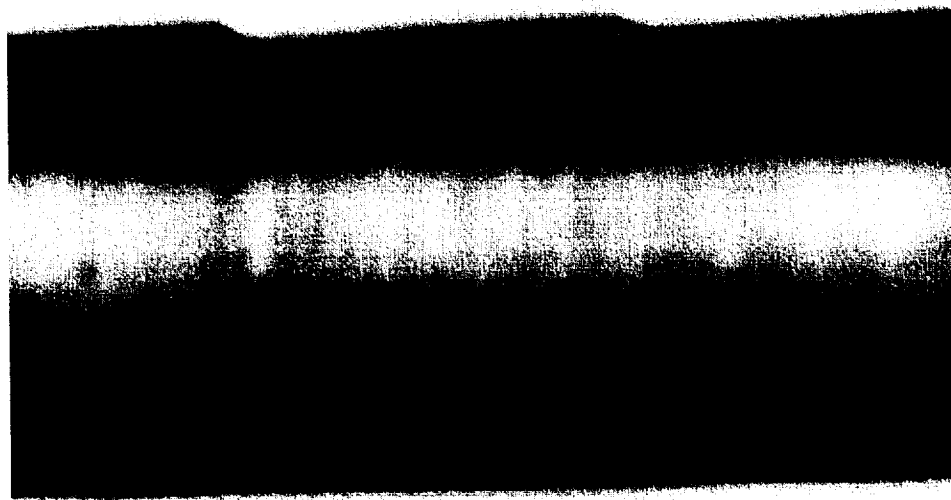


Figure 2: Schematic of the Brillouin spectroscopy system (BS = beam splitter, M = mirror, L = lens, FL = focusing lens, CL = collecting lens, PH = pinhole, PR = prism, FPC = Fabry-Perot controller, OSC = oscilloscope, MCA = multichannel analyzer, PC = Personal Computer, FPP = Fabry Perot Plates)

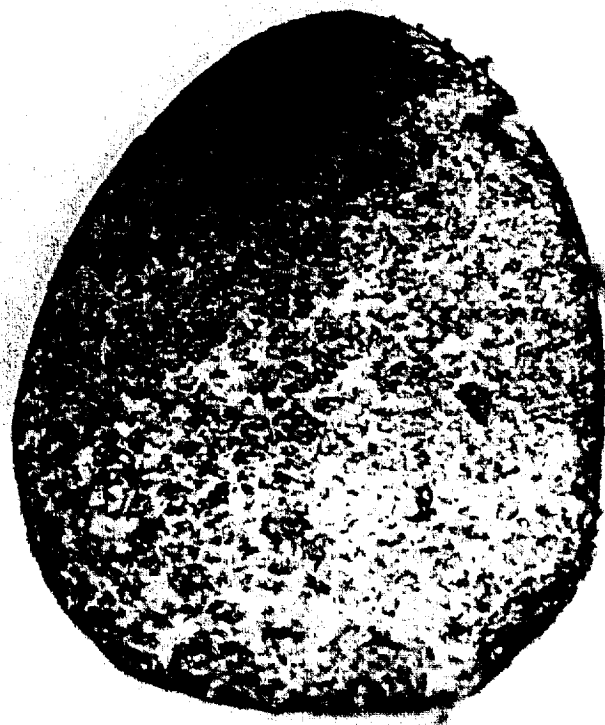




500μm



a)



500μm



b)

Figure 3: Optical micrographs of mullite sample (a) lengthwise and (b) in cross section

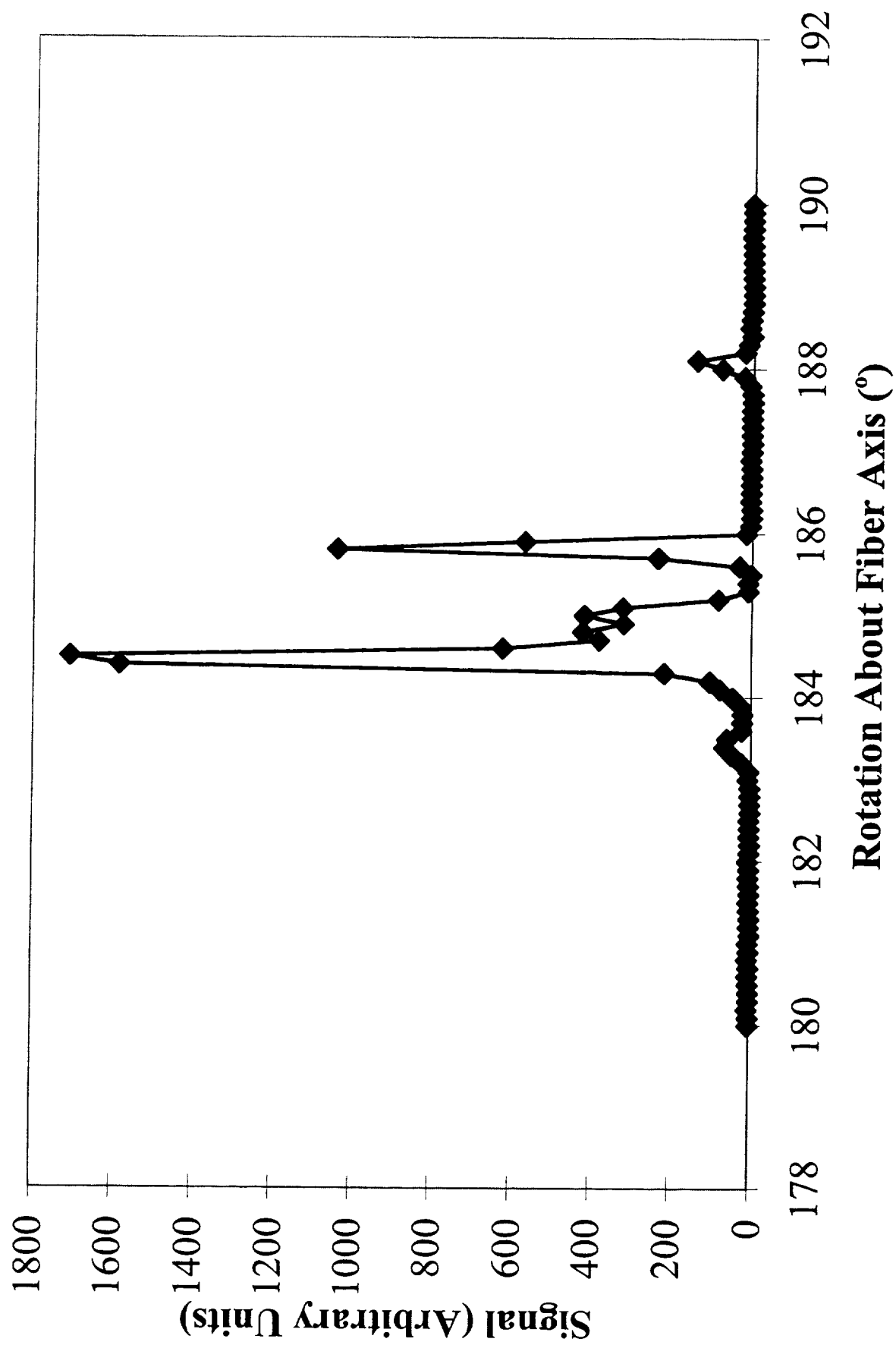


Figure 4: X-ray scan rotating sample around fiber axis with fixed  $2\theta$

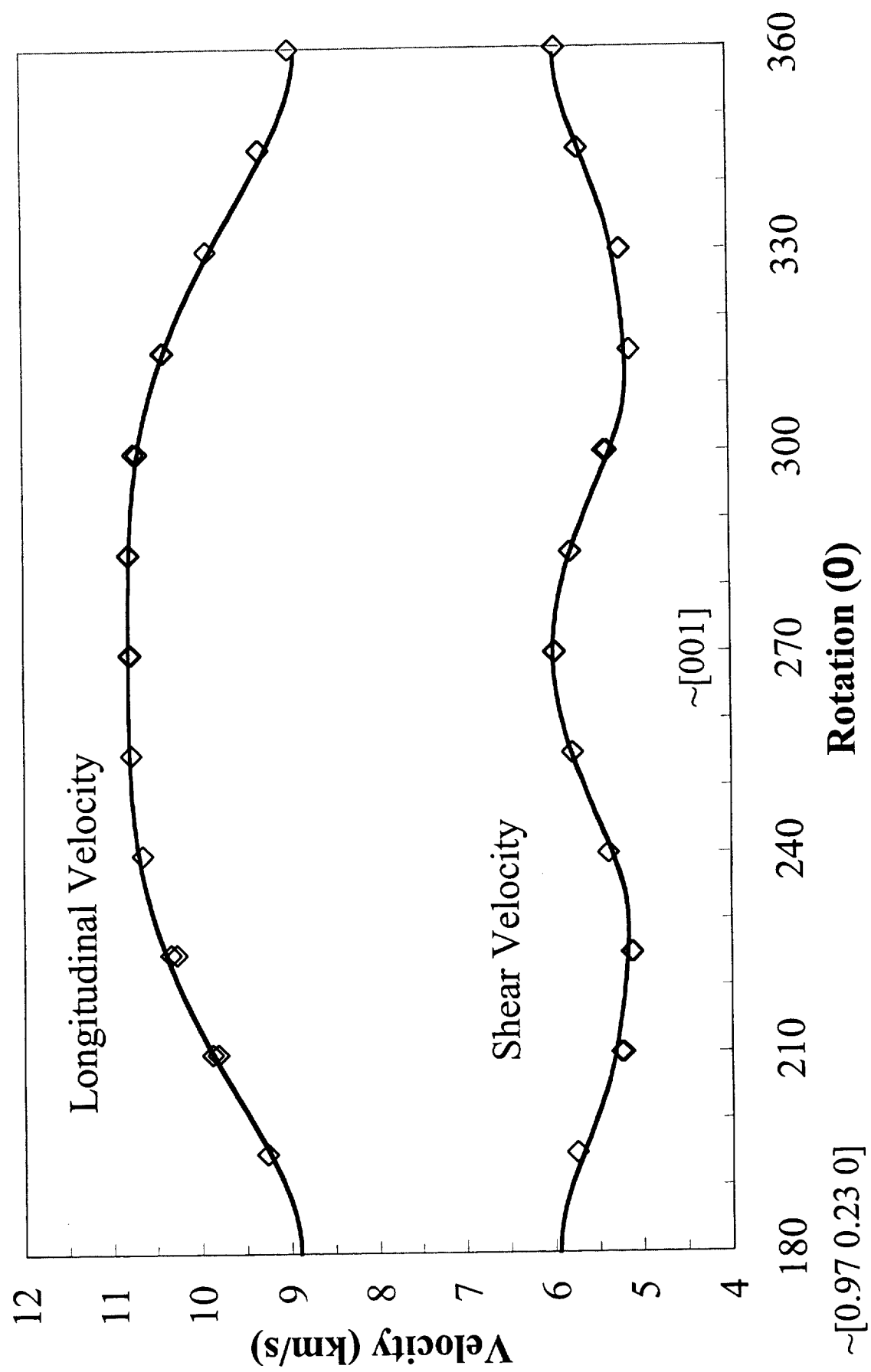


Figure 5: Room temperature velocities versus rotation in  $\sim(100)$  plane

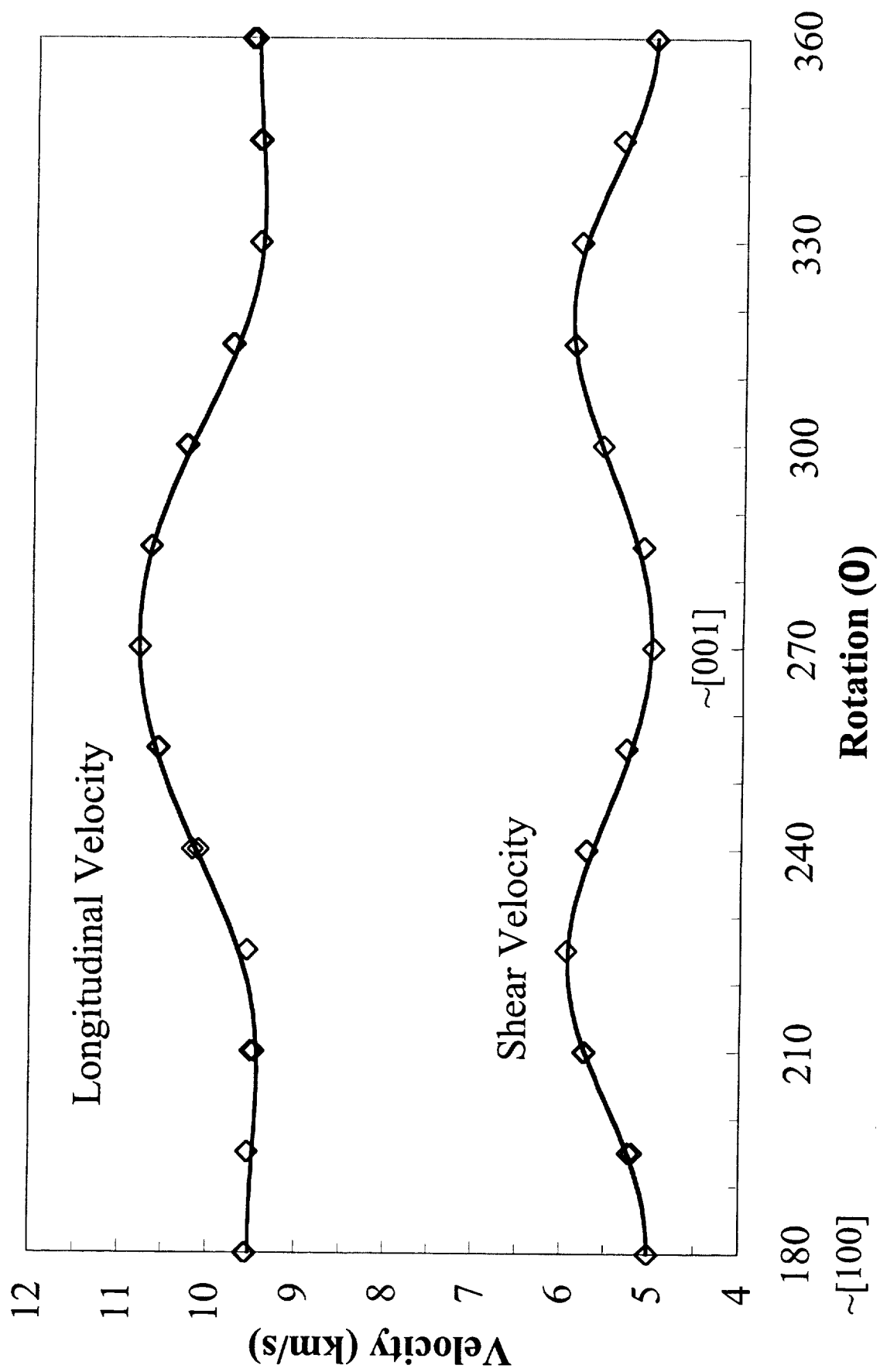


Figure 6: Room temperature velocities versus rotation in  $\sim(010)$  plane

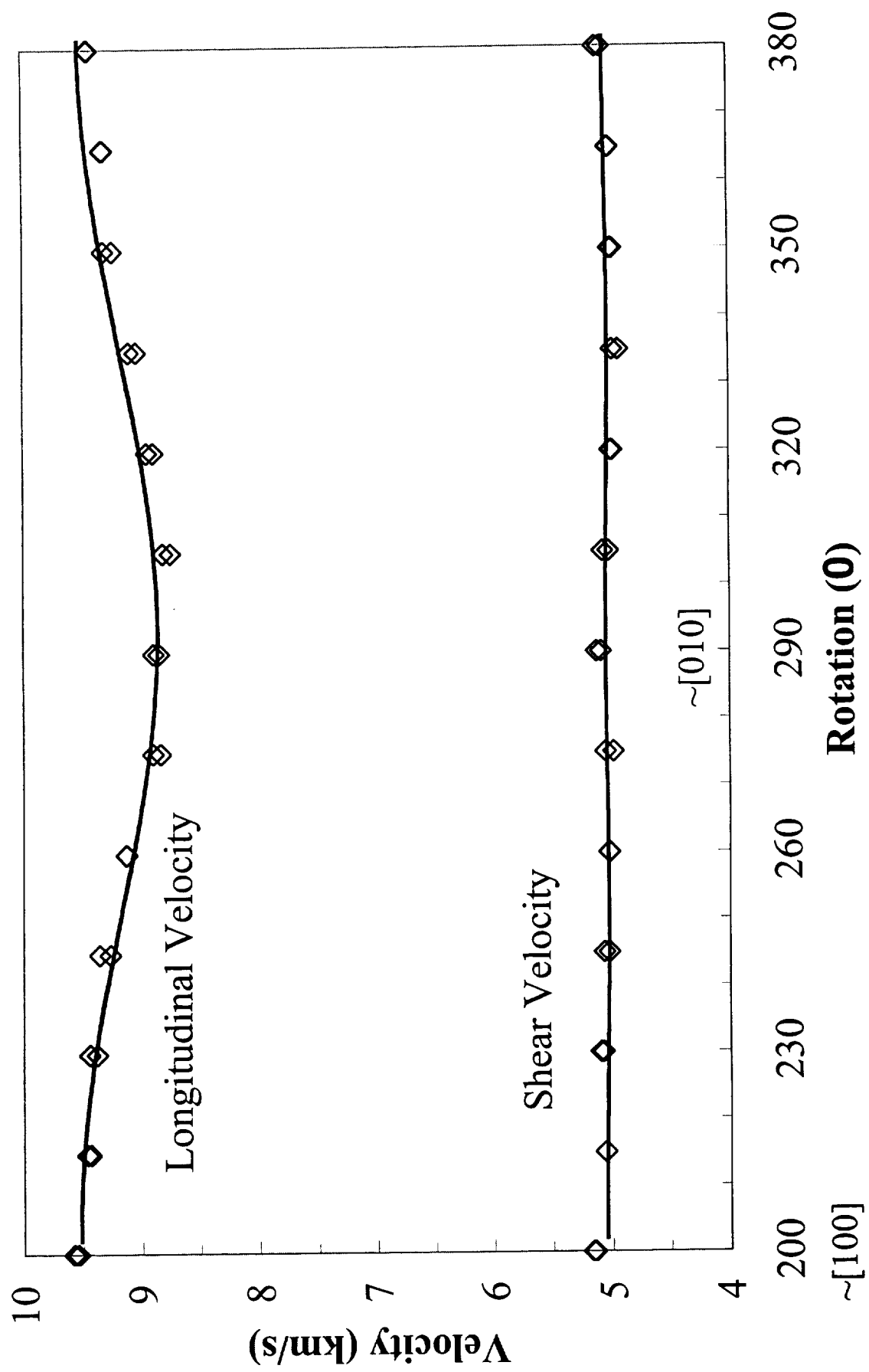


Figure 7: Room temperature velocities versus rotation in  $\sim(001)$  plane

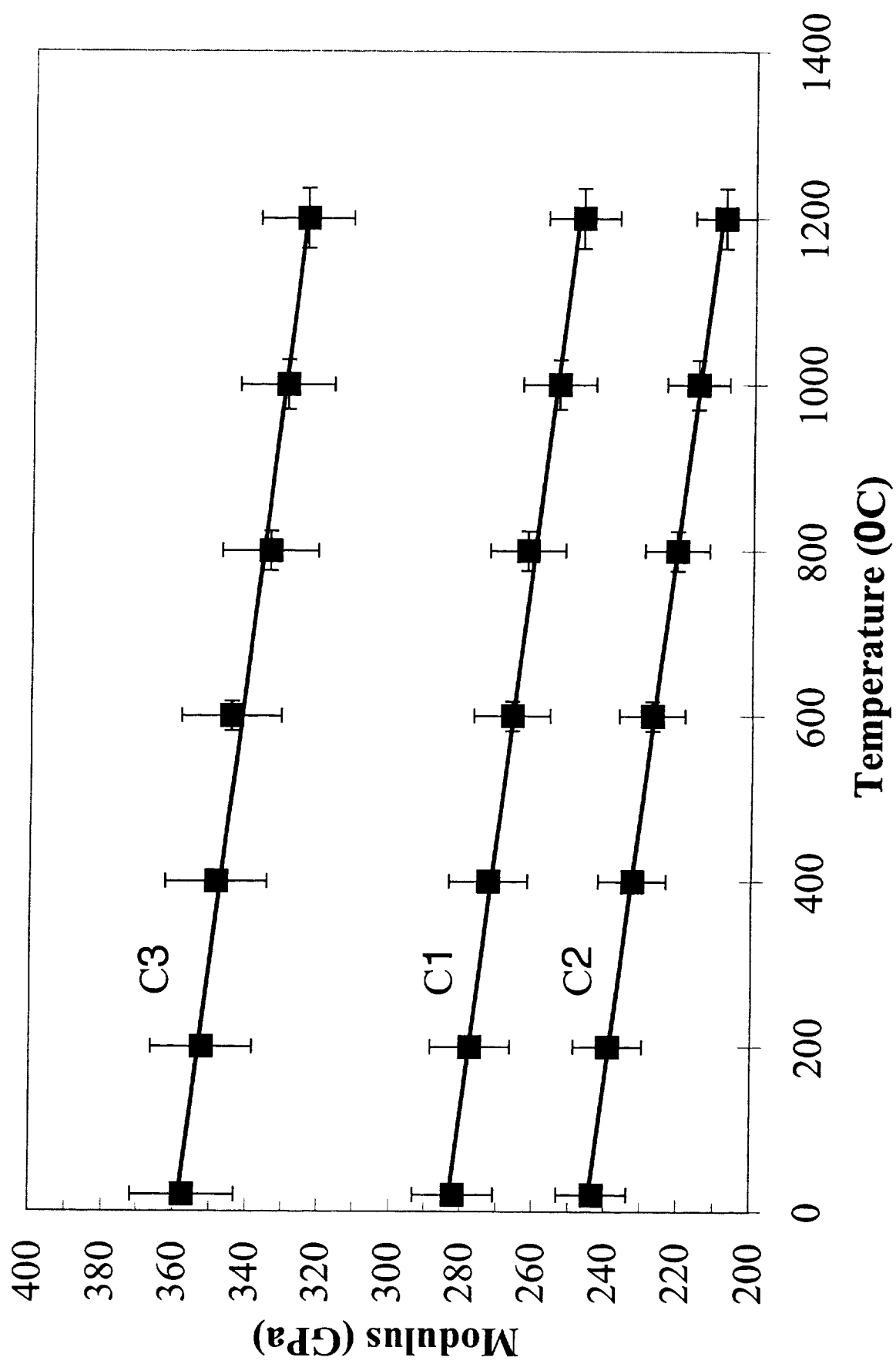


Figure 8: Single-crystal longitudinal moduli versus temperature

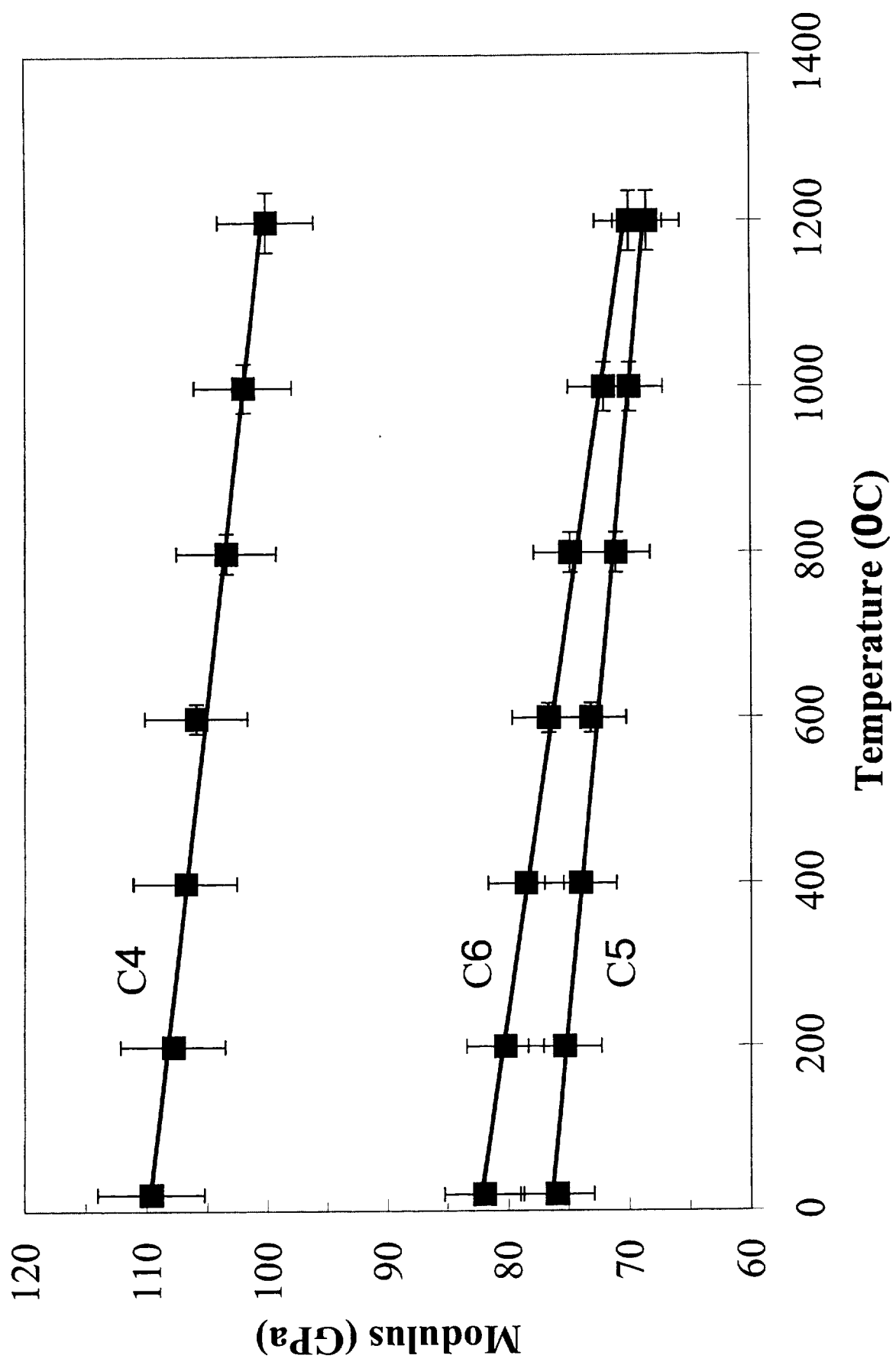


Figure 9: Single-crystal shear moduli versus temperature

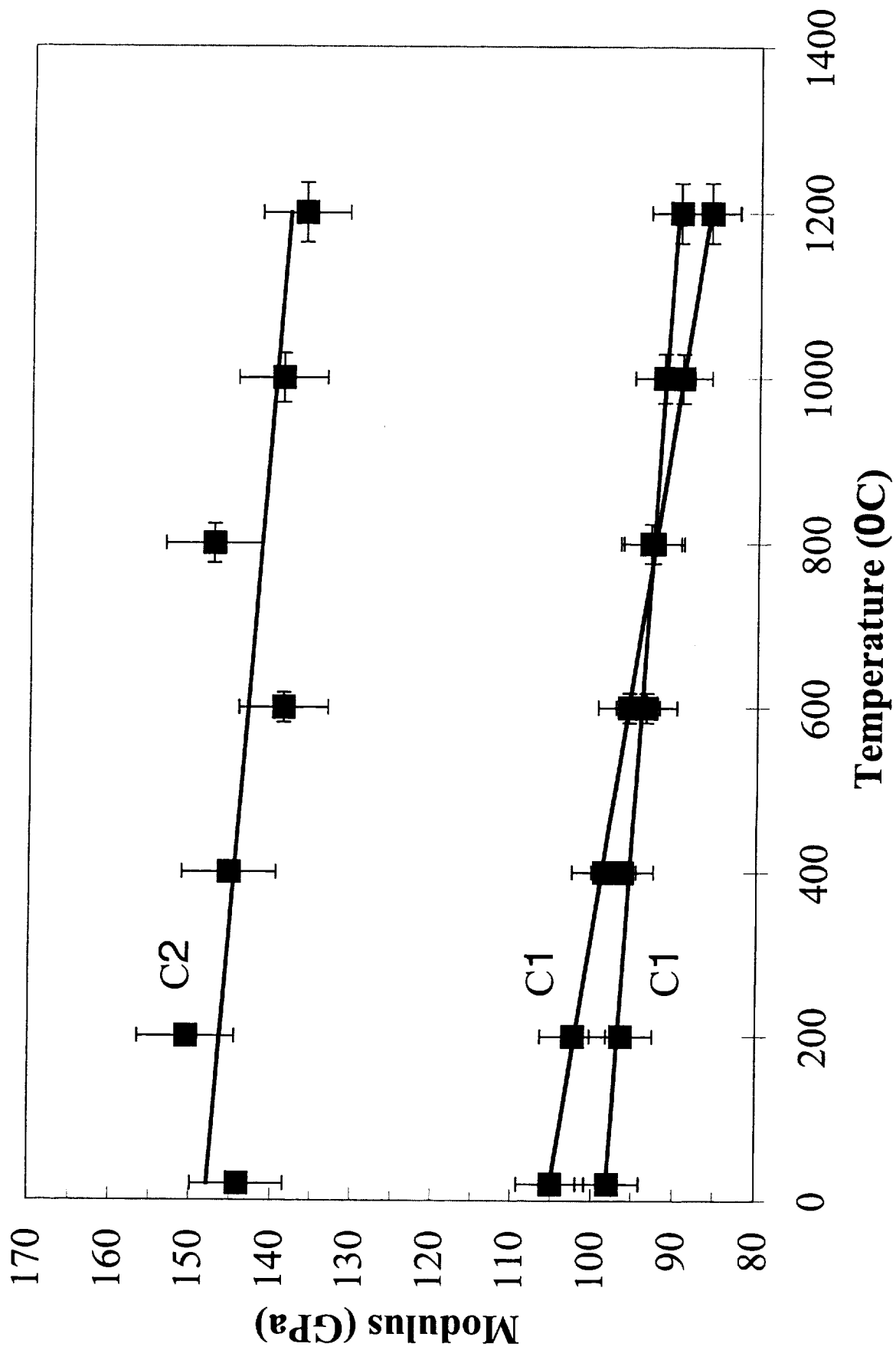


Figure 10: Single-crystal cross moduli versus temperature



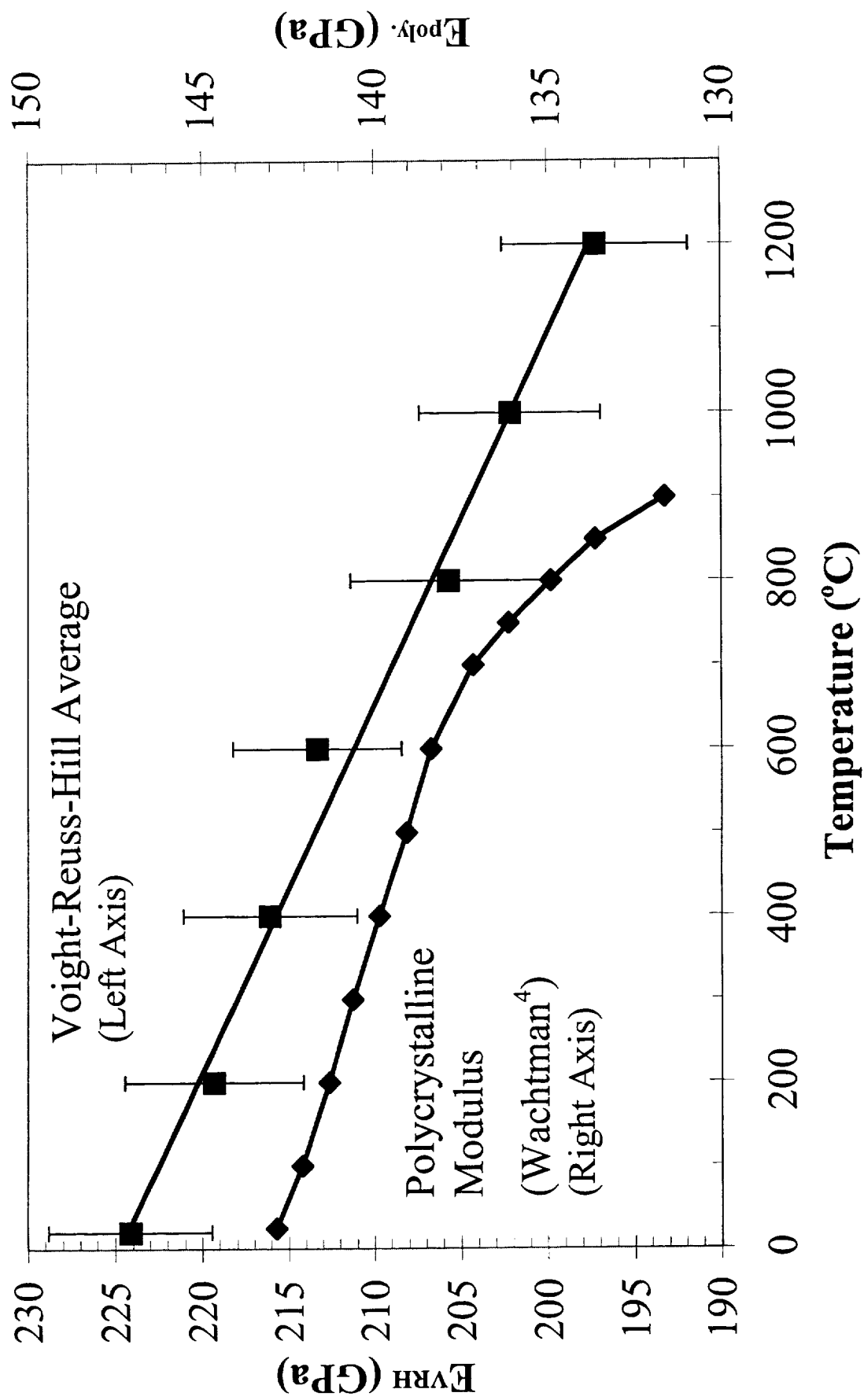


Figure 11: Young's modulus of mullite versus temperature

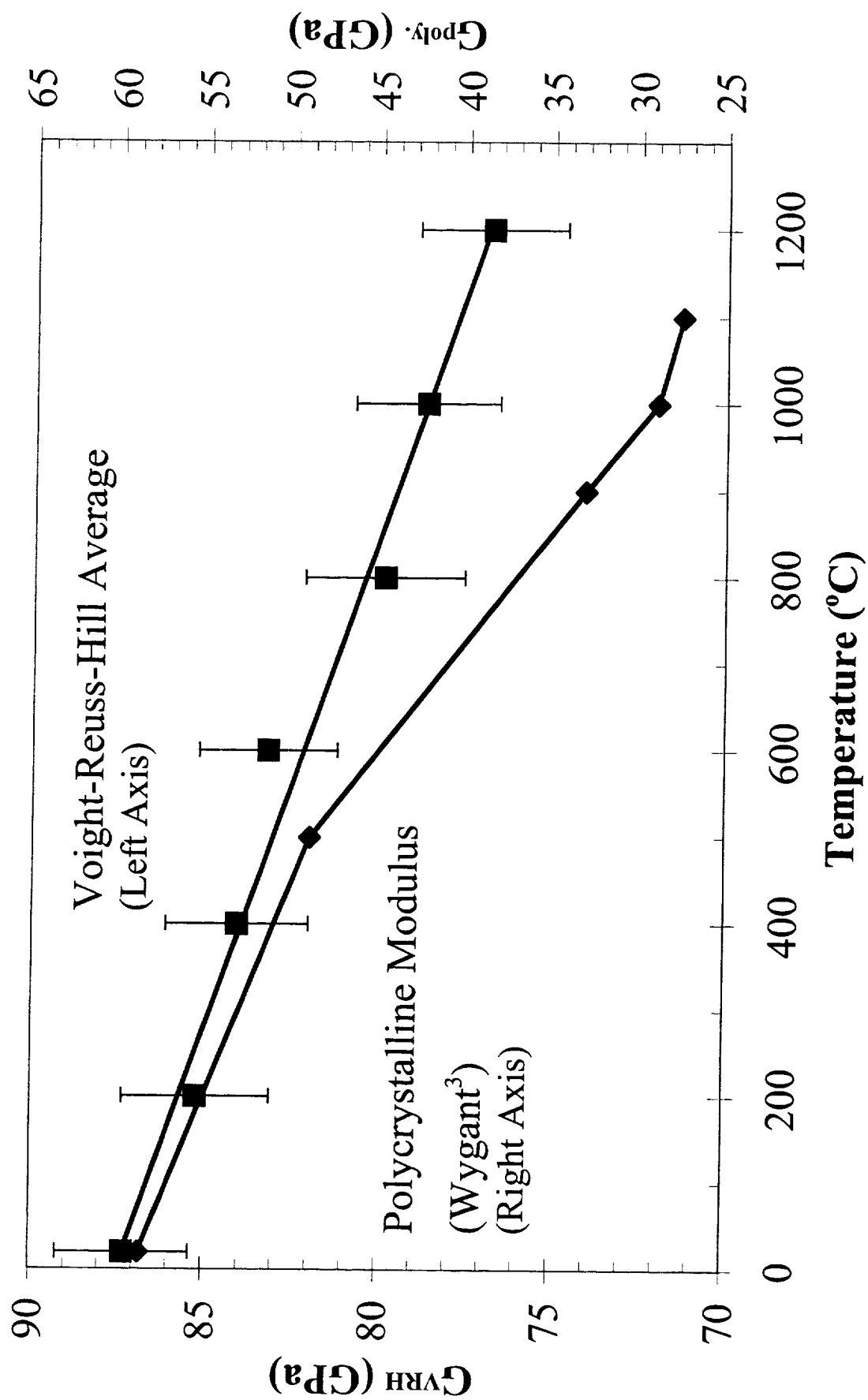


Figure 12: Shear modulus of mullite versus temperature

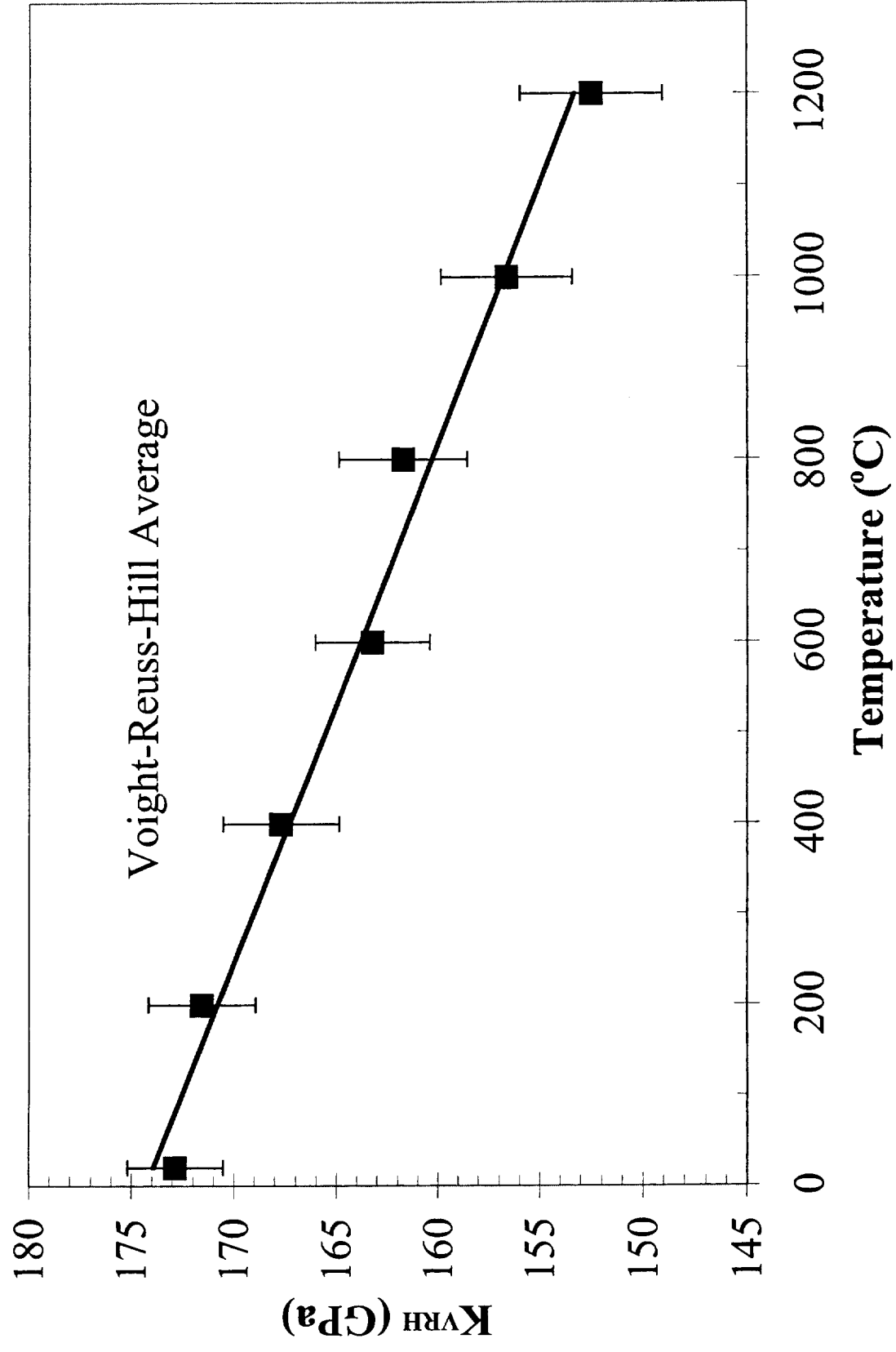


Figure 13: Bulk modulus of mullite versus temperature

